Antireflection High-Index Metasurfaces Combining Mie and Fabry-Pérot Resonances

Andrea Cordaro,[†,‡,§,∥] Jorik van de Groep,[†] Søren Raza,[†,⊥] Emanuele Francesco Pecora,[†] Francesco Priolo,[‡,§] and Mark L. Brongersma*,[†]

[†]Geballe Laboratory for Advanced Materials, Stanford University, Stanford, California 94305, United States
[‡]Dipartimento di Fisica e Astronomia "Ettore Majorana", Università di Catania, via S. Sofia, 64, 95123 Catania, Italy
[§]Scuola Superiore di Catania, Università di Catania, via Valdisavoia, 9, 95123 Catania, Italy
[⊥]Department of Physics, Technical University of Denmark, DK-2800 Kongens Lyngby, Denmark

Ⓢ Supporting Information

ABSTRACT: Minimizing reflection losses is required for the efficient operation of a wide range of optical components. Antireflection coatings supporting Fabry-Pérot resonances are commonly used to solve this problem and can be applied on an industrial scale. Recent work has shown that reflections can also be reduced by placing an array of high-index nanostructures on a surface. In such coatings, antireflection is achieved by tailoring the scattering by optical Mie resonances. Here, we design and fabricate Si metasurfaces that combine both Fabry-Pérot and Mie resonances in a single metasurface to realize a multiresonant broadband antireflection response. We optically characterize the metasurfaces demonstrating 4.1% AM1.5-averaged reflectance across the visible spectrum (425−900 nm). Our metasurface design strategy is generally applicable to different materials and frequency ranges, making our approach relevant for a broad variety of applications.

KEYWORDS: metasurface, anti-reflection coating (ARC), Mie resonators, effective medium, Fabry-Pérot resonances
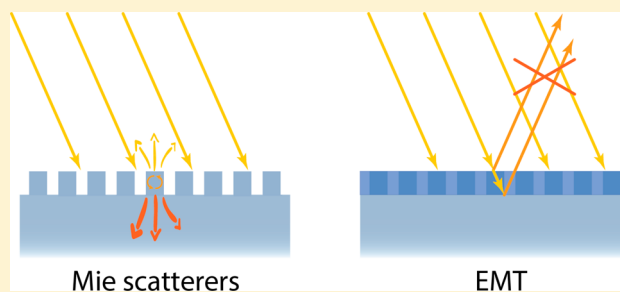
The quest for more efficient photonic devices relies on our ability to manage the flow of light at the nanoscale. In this work, we analyze whether Mie resonant nanostructures can help reduce unwanted reflections at material interfaces, arguably the most ubiquitous problem in the design of optoelectronic devices. For photovoltaic applications, the design of antireflection (AR) coatings is particularly challenging as it needs to be achieved across a very broad spectral range.

The minimization of reflection of a flat substrate was first demonstrated by placing a thin layer of transparent dielectric, referred to as Rayleigh's film,[1] at the interface of the substrate to suppress reflection by destructive interference.[2] However, a major disadvantage of such single-layer interference coatings lies in the strong dependence on both the angle of incidence and the wavelength of the incident light. Further evolutions of the interference AR concept include multiple or graded-index coatings,[3−7] achieving broadband and omnidirectional AR at the expense of ease of fabrication and costs.

Novel approaches exploit high-index resonant scatterers[8] and optical metasurfaces[9,10] to achieve broadband antireflection. These are arrays of low-aspect-ratio nanostructures that can conveniently be patterned by a variety of approaches. When properly sized, they can effectively capture and redirect light through the excitation of optical Mie resonances.[11−15]

This enables strong forward scattering[16,17] of incident light into the substrate to reduce reflectance.[18,19] However, the spectral efficiency of these nanopatterns is limited by their resonance bandwidth, and a multiresonant behavior is needed in order to cover the majority of the solar spectrum.[8,20]

Here, we demonstrate how silicon (Si) metasurfaces can combine the beneficial effects of Fabry-Pérot (FP) resonances and Mie resonances in a single layer. To this end, we carefully arrange nanowires or pillars into subwavelength arrays to achieve broadband and spectrally engineered antireflection. Using a simple theoretical model based on coupled mode theory (CMT),[21−25] we develop an intuitive insight into the multimodal interaction between the FP and Mie resonances within the nanopatterned layer. Our experimental results demonstrate broadband antireflection in the spectral range from 425−900 nm for optimized designs. The multiresonant metasurface concept can be generalized to all high-index materials and other wavelength ranges, making it suitable for a broad range of applications including solar cells, sensors, and other optical components.
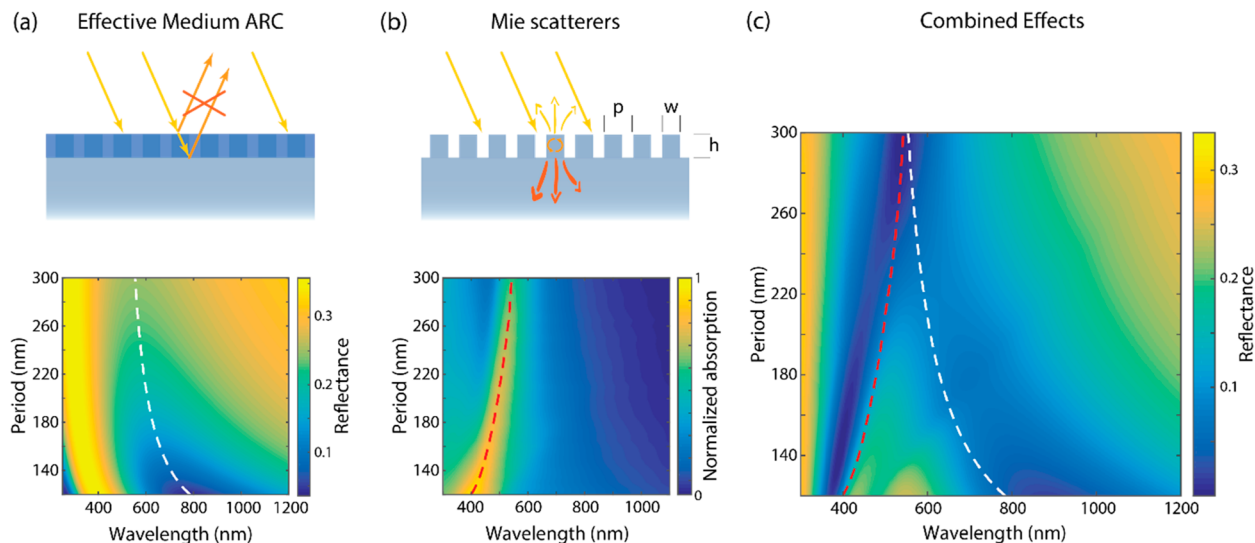
Figure 1. Antireflection behavior of Mie-resonant antireflection coatings supporting Fabry-Pérot and Mie resonances. (a) Analytically calculated reflectance of a slab of index n_{eff} on a substrate with index $n_{Si} = 4 + 0.1i$ as a function of the period p (and thus n_{eff}) and wavelength λ. (b) The importance of a Mie resonance is seen in the simulated spectral absorption in Si nanobeam arrays placed on a Si substrate. A schematic of the structure illustrates the excitation of a Mie resonator. The beam width is chosen as 80 nm and the height as 120 nm for all of the panels in this figure. (c) Simulated reflectance of an array of Si nanowires on a substrate as a function of p and λ.

■ THEORY

In this section, we introduce the concept of a multiresonant metasurface in which FP and Mie resonances can be made to work together to reduce reflection. The initial starting point is to leverage the work on conventional thin interference AR coatings to achieve a low reflectance across a broad range of wavelengths in the red side of the solar spectrum. Then, we will use the knowledge of Mie resonators to carve a second reflectance minimum at shorter wavelengths in order to achieve an overall more broadband antireflection in a single effective layer.

Whereas traditional AR coatings have been continuous films of a single material (e.g., Si₃N₄), more flexibility to control the refractive index has come from the use of deep-subwavelength nanostructures forming a metamaterial with an effective index. To illustrate this concept, we first consider a dense array of Si nanobeams placed on a Si substrate. When the spacing of the nanobeams is made sufficiently small compared to the illumination wavelength, the array functions as an effective medium supporting a FP resonance. The location of this resonance depends on the layer's effective index n_{eff} that is controlled by the refractive indices of the constituents (n_{air} and n_{Si}) as well as by their filling fractions.[26] To first order, the magnitude of n_{eff} is described by effective medium theory. For anisotropic nanobeam arrays, the effective index depends on the polarization of incoming light as[27]

$$n_{eff}^{\perp} = \left(\frac{1 - F}{n_{air}^2} + \frac{F}{n_{Si}^2} \right)^{-1/2} \quad n_{eff}^{\parallel} = [(1 - F)n_{air}^2 + Fn_{Si}^2]^{1/2} \tag{1}$$

where $n_{eff}^{\perp}$ is used when the electric field **E** is polarized perpendicularly to the wire axes (TE polarization) and $n_{eff}^{\parallel}$ is used when **E** is polarized along the wire axes (TM), and F is the filling fraction of Si. For most practical purposes, a polarization-independent geometry based on, for example, nanopillars is more relevant. In the latter case, the effective index is given by the root-mean-square of $n_{eff}^{\perp}$ and $n_{eff}^{\parallel}$.[28] To highlight the key physics, we first consider a constant refractive

index $n_{Si} = 4 + 0.1i$ to avoid complications from the material dispersion in real Si. Figure 1a shows the analytically calculated reflectance of a slab of thickness $h = 120$ nm, with index given by eq 1 (with $n_{air} = 1$) as a function of the filling fraction (directly related to the periodicity). Reducing the period from 300 to 120 nm for a fixed wire width (80 nm) shifts the minimum to longer wavelengths. At the same time, the minimum becomes lower as n_{eff} increases and gets closer to the ideal AR condition $n_{eff} = \sqrt{n_{air}n_{Si}}$. The interference coating thus forms a single broad dip in reflection as a result of a broad Fabry-Pérot resonance.

Recent work has demonstrated that high-index nanostructures with sizes comparable to the wavelength of light in the medium support optical Mie-type resonances[11−15] whose spectral location can be tuned with both the nanobeam height and width.[29] For 80 nm wide and 120 nm high beams, the lowest-order Mie resonance (Magnetic Dipole) appears near the peak of the solar spectrum at 500 nm[17] (Figure 1b). As a result, light at this wavelength is efficiently scattered forward into the substrate, lowering reflection.

According to the above discussion, it is clear that a dense array of nanobeams can support two pathways for an incident light wave: a FP resonant pathway governed by the effective-index layer just described (Figure 1a) and a Mie-resonant pathway (Figure 1b). In order to investigate the interplay of the two pathways, Figure 1c shows the simulated (Lumerical FDTD[30]) reflectance spectra of an array of nanobeams under normal incidence (TE polarized) as a function of the periodicity p. Only one reflection minimum is observed at larger periodicities, while another dip appears as the array periodicity is reduced. This provides for a broader and more efficient antireflection behavior.

To identify the origin of the two minima, two dashed lines are added to Figure 1c indicating the resonance wavelength of the isolated mechanisms (Figure 1a,b). The red dashed line marks the peak of the power absorbed within the wires (Figure 1b), which is a good indication of the system's Mie resonance wavelength as a function of the array periodicity. For small
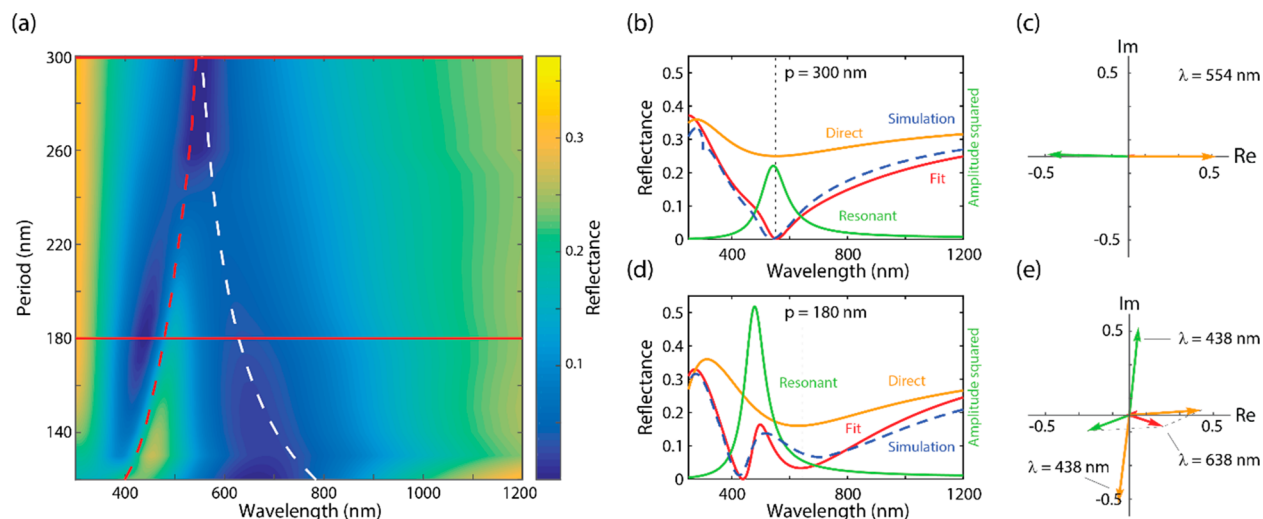
Figure 2. Coupled mode theory for Mie-resonant antireflection coatings. (a) CMT-modeled reflectance map obtained by fitting to the spectral reflection data obtained by FDTD simulations, as shown in Figure 1c. (b, d) Comparison between simulated (dashed blue) and CMT-fitted spectra (red) for an array of nanowires (w = 80 nm, h = 120 nm) for p = 300 nm (b) and p = 180 nm (d). Square modulus of the direct (yellow) and resonant (green) pathways composing the fits are also shown. Note that the label "Reflectance" does not apply to the resonant pathway. (c, e) Phasor diagram representation of the two pathways at the wavelengths of the minima (dashed lines) in (b) and (d).

periods, the magnetic dipole modes in neighboring wires couple, giving rise to a blue-shift. Hence the red dashed line indicates the spectral location where the Mie resonant pathway dominates. On the other hand, the dashed white line (Figure 1a) indicates the reflectance minimum as a function of filling fraction and helps to identify the FP pathway in Figure 1c. Based on the broader spectral properties of the FP resonance, we will refer to the FP related feature as the Fabry-Pérot background.

It is important to stress that the position of the minima in Figure 1c does not necessarily coincide with the minima that the two pathways would generate individually. In fact, the interference of the broad FP background and the Mie resonance can give rise to a characteristic asymmetric Fano line-shape.[31] For such a resonance, the distance between the minimum of the spectrum and the resonant frequency depends on the so-called Fano shape parameter, which describes the degree of asymmetry.[32,33] Moreover, the second minimum is slightly shifted compared to that of the FP background alone due to the presence of the Mie resonance. To achieve the best antireflection, it is clear that the relative amplitude and phase of the light scattered fields produced by each mechanism will need to be optimized. We use coupled mode theory to quantitatively explore the interaction of the two resonant mechanisms. CMT is very powerful in describing the behavior of coupled resonances and enables the possibility of calculating the reflectance of an optical system by modeling its interaction with incident light through different resonant processes.[21−25] The reflectance of the coupled system is given by (see Supporting Information):

$$R = \left| r_{\text{eff}} + \frac{Ae^{i\phi}}{i(\omega - \omega_0) + g} \right|^2 \quad (2)$$

Here, r_{eff} is the Fresnel reflection coefficient for a dielectric slab of index n_{eff} on a substrate. The parameters ω_0, A, ϕ, and g determine the resonance frequency, amplitude, phase offset, and width of the Lorentzian function in the second term. The first term represents the broader FP background, while the

second term corresponds to the Mie-resonant pathway with a Lorentzian line shape. To capture the antireflection behavior over a broader wavelength range or with different particle sizes, additional Mie resonances may be added.

To demonstrate that the doubly resonant nature observed in Figure 1 is well-described by CMT, we explore whether the full-field simulated spectra can be captured by eq 2. A quick inspection of eq 2 reveals that the dependent parameters are n_{eff}, ω_0, A, ϕ and g. Given the large number of parameters, it is of value to obtain physically reasonable values for as many of them as possible. As mentioned, n_{eff} is a function of the Si filling fraction and a reasonable estimate of ω_0 can be obtained from the frequency of maximum absorption within the wires (Figure 1b). Based on these assumptions, the spectra composing Figure 1c are then fitted to generate Figure 2a. Despite its simplicity and approximations (see Supporting Information), the agreement between the CMT model and the full-field simulations across many periods and wavelengths suggests that it captures the key physics. As such, it is a useful tool to optimize the broadband antireflection of these types of coatings.

Due to the complex-valued nature of the two terms in eq 2, antireflection behavior at multiple spectral locations is not obtained by simply adding two pathways that would generate a dip in reflectance when isolated (in accordance with the observations in Figure 1). To fully exploit the doubly resonant nature of our structure, the amplitude of the two pathways must match with a π phase difference. To evaluate whether these conditions are met, two spectra in the single-dip and double-dip regime are isolated (p = 300 and 180 nm, respectively) and plotted along with the amplitude of the corresponding FP (yellow) and Mie resonant (green) pathways (Figure 2b,d). The spectra obtained from the full-field simulations are also shown (blue dashed), demonstrating good correspondence with the CMT fit (red). For p = 300 nm (single-dip regime) the FP and Mie resonant pathways are almost equal in amplitude on resonance (λ = 554 nm, Figure 2b). To study the relative phase at resonance, a phasor diagram is used to simultaneously plot the amplitude and phase for the

two pathways in the complex plane (Figure 2c). The resulting reflectance (red) can be obtained by vectorial addition of the direct (yellow) and resonant (green) components. Figure 2c clearly demonstrates that the two pathways are close to equal in amplitude and π out of phase simultaneously, giving rise to a low reflectance. For the period of 180 nm, a double-dip occurs and the interference between the two pathways gives rise to a characteristic asymmetric Fano line-shape superimposed on the broad FP background. The amplitude is matched twice (Figure 2d) but the AR condition is perfectly satisfied only for the first dip (λ = 438 nm). The second dip is slightly red-shifted with respect to the second amplitude-matching wavelength, and the phase difference between the pathways is slightly less than π (Figure 2e). As a result, the reflection is not completely canceled.

Finally, both resonant mechanisms and, therefore, the entire reflectance spectrum can be designed at will through careful engineering of the nanostructure dimensions (see Supporting Information). For example, increasing the height of the wires results in a thicker effective layer, shifting the dip in the Fabry-Pérot background to longer wavelengths. On the other hand, changing the dimension of the nanobeams also results in a change in the Mie resonant properties[17] and the position of the associated dip. Hence, our structure's design is not carried out by simple numerical minimization of the average reflectance but is rather obtained through judicious design of the interplay of the two mechanisms using our theoretical model.

■ EXPERIMENTAL SECTION

To demonstrate the doubly resonant metasurface AR-coating experimentally, we fabricate an optimized metafilm based on a Si nanobeam array and measure its reflection spectrum. Using the dispersive index of silicon[34] and aiming to place both reflection dips within the visible spectrum, the designed geometry for polarized light is a nanowire array with w = 80 nm, h = 120 nm, and p = 180 nm (see Supporting Information). The structures were fabricated by electron-beam lithography. Si substrates were spin-coated with an 80 nm thick layer of hydrogen silsesquioxane negative e-beam resist (HSQ, 4% in methyl isobutyl ketone), and baked for 45 min at 90 °C. Lines were fabricated in the HSQ by exposure using a JEOL JBX 6300 lithography system (100 kV, dose 1500−3500 $\mu C/cm^2$) and development in tetramethylammonium hydroxide (TMAH 25%, 120 s). The pattern was then transferred into the Si by a two-step reactive-ion etching procedure using C_2F_6 and Cl_2/HBr, respectively. Finally, the cross-linked HSQ mask was removed using HF (5% in H_2O). The resulting nanobeam array is composed of smooth Si beams that are uniform in size across a large area (Figure 3a). The focused-ion-beam (FIB) cross-section shows slight slanting of the walls with a width that is changing from top to bottom from about 65 to 115 nm (Figure 3b). The height of the beams is about 145 nm, as determined by atomic force microscopy (AFM; Figure 3c). We measure the local reflectance spectrum with a Nikon C1Si Confocal Microscope equipped with a Princeton Instruments SpectraPro 2300i spectrometer and PIXIS CCD-detector. We use a 20X objective (Nikon, NA = 0.4) and a 100 μm pinhole to analyze the reflectivity of the nanobeam array across the 425−900 nm spectral range. We employ a silver-coated mirror (Thorlabs PF10-03-P01) as a reference. Also, the microscope's aperture diaphragm (A-stop) is closed to ensure the smallest incident
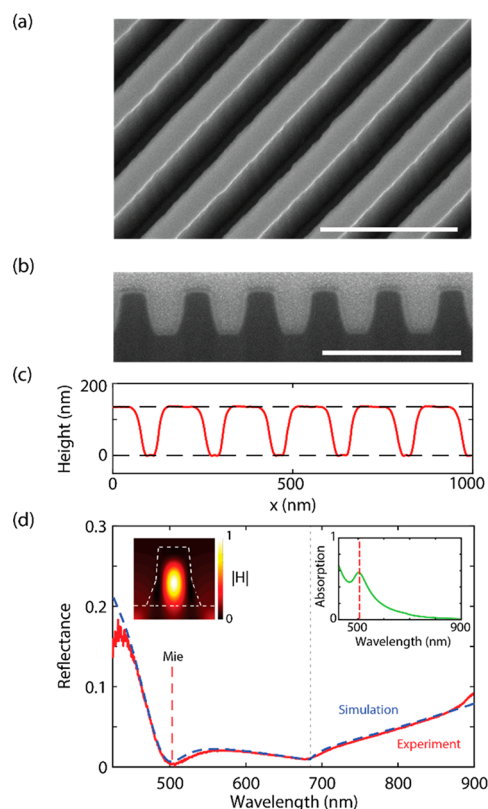

Figure 3. Fabrication and optical properties of a Mie-resonant antireflection coating composed of Si nanobeams. (a) Tilted SEM image of the Si nanobeam array. (b) SEM image of a FIB cross section of the same nanobeam array shows slight slanting of the side walls. The scale bars in (a) and (b) are 400 nm. (c) Depth profile analysis obtained from an AFM line scan. (d) Experimental (red) and simulated (dashed blue) reflection spectra. Insets: magnetic field amplitude profile and absorption within the nanobeam volume. The dashed vertical red line denotes the location of the Mie resonance, while the dashed black line indicates the onset of diffraction in the substrate.

angle possible, and a polarizer in the collection path is used to analyze just the TE polarized light reflection.

The measured reflectance spectrum (red, Figure 3d) experimentally demonstrates the double-dip in reflectance as a result of the doubly resonant behavior of the metasurface AR coating. First, a minimum located at 500 nm due to the magnetic dipole resonance in the individual wires is present. To corroborate this, the simulated absorption within the nanowires is shown as an inset, which exhibits a clear peak around λ = 500 nm due to resonant absorption. The magnetic field amplitude at resonance is also shown, with the characteristic magnetic dipolar profile clearly observable. Second, a spectrally broad minimum is observed between 600 < λ < 800 nm due to the FP resonance. The kink in reflectance close to 700 nm is due to a Rayleigh anomaly at the diffraction edge. Using the actual dimensions and shape extracted from FIB cross sections and AFM line scans to account for fabrication imperfections, it is possible to compare the experimental spectrum to its FDTD-simulated counterpart using the dispersive index of silicon.[34] The resulting spectrum (blue dashed, Figure 3d) shows very good correspondence to the experimental spectrum. Broadband AR is obtained from two separate spectrally engineered resonant modes within the same metasurface coating, with an averaged experimental

reflectance as low as 3.9% in the wavelength range from 425–900 nm (weighted for the AM 1.5 solar spectrum). The experimentally observed double-dip is not as evident as in the theory (Figure 2d), and this can be understood by assessing the impact of fabrication imperfections on the reflectance of our structure, as discussed in depth within the next section.

The results thus far demonstrate how anisotropic structures, like the arrays of Si nanowires in Figure 3a, can combine two resonant mechanisms to obtain broadband AR for polarized light. Most practical applications, however, require efficient AR for unpolarized light. To demonstrate the multiresonant metasurface concept for unpolarized light, we design an array of square-based nanopillars with w = 90 nm, h = 115 nm, and p = 150 nm. Figure 4 displays the structural and optical
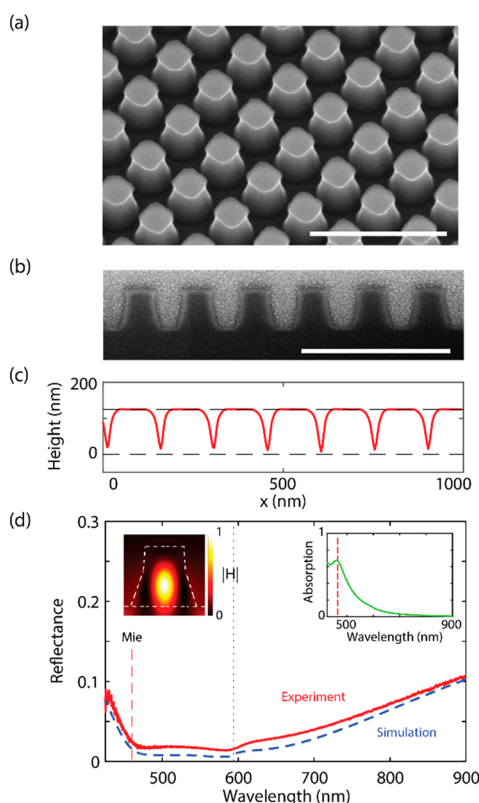

Figure 4. Fabrication and optical properties of a Mie-resonant antireflection coating composed of Si nanopillars. (a) Tilted SEM image of the nanopillar metasurface. (b) SEM image of a FIB cross section of the nanopillar array. The scale bars in (a) and (b) are 400 nm. (c) Depth profile analysis obtained from AFM line-scan. (d) Experimental reflectance spectrum for unpolarized light (red) and simulated (dashed blue) counterpart using the dispersive index of Si.[34] Insets: magnetic field amplitude profile and absorption within the nanopillar volume. The dashed vertical red line denotes the spectral location of the Mie resonance while the dashed black line indicates the onset of diffraction in the substrate.

characterization of the fabricated nanopillar array. Similar to the nanowires array, SEM and FIB analysis reveal a good sample uniformity with some slanting of the sidewalls (Figures 4a,b). Combining FIB cross sections and AFM line scans (Figure 4c) the measured as-fabricated dimensions are h = 125 nm and a width varying from 75 nm at the top of the pillars to 115 nm at the bottom. As with the nanobeam array, the slanting strongly affects the optical response of the metafilm (Figure 4d). Although the double-dip is not visible, it is still

possible to distinguish the same features that characterize the nanobeam array reflectance spectrum: around 450 nm the Mie mode (shown as inset) is producing an extra dip in the broad spectral reflectance curve due to the FP resonance. A kink around 600 nm again marks the onset of diffraction into the substrate. The absence of the double-dip is due to the fact that the two pathways are spectrally closer compared to the case of the nanobeam array. However, this proves to be beneficial to the overall performance of our structure showing a 4.1% AM1.5-averaged reflectance for unpolarized light. Again, the agreement between simulation and experiment is good and only small deviations result from a nonperfect capture of the exact shape/dimensions of the metafilm. Altogether, the good agreement seen between experiment and simulations suggests the value of multiresonant metasurfaces in suppressing reflection both for polarized and unpolarized light.

◼ DISCUSSION

The overall good agreement between experiment and simulations could only be obtained by taking into account the slanting of the sidewall of the Mie resonators produced by the reactive-ion etching process. Its notable impact on the reflectance properties raises the question whether the sidewall slant can be engineered to further increase the performance of Mie-resonant AR coatings. Figure 5a shows the simulated spectral reflectance (color) of an as-designed Si nanobeam array (w = 80 nm, h = 120 nm, and period p = 180 nm) as a function of the sidewall slant angle. Specifically, the sidewalls of the structures were slanted while keeping both the height and the width at half height constant. Figure 5b shows cross cuts of resulting trapezoidal cross-sectional shapes (a) for straight walls (slanting of 0 nm) and for increasing values of slanting. The striking feature in Figure 5a is that the two dips, the result of the different resonant mechanisms, merge into a broad single dip with increasing slanting. In fact, the reflection at the merged minimum (at 15 nm slanting, corresponding to a slanting angle of 14 degrees) is remarkably low. To investigate this phenomenon, the effects of slanted sidewalls on the resonant and on the direct pathways are analyzed separately. The Mie-resonant pathway is broadening and red-shifting with increased slanting (Supporting Information). The characteristic displacement current loops of the magnetic dipole mode move into the substrate as the sidewalls acquire a slant. As a result, the resonator-to-substrate coupling is stronger and the leakage rate into the substrate increases, giving rise to a broadening of the resonance. In addition, the lateral dimension of the currents loops increases with slanted sidewalls. As a consequence, the effective resonator width increases and its resonance wavelength red-shifts. On the other hand, the FP resonant pathway through the slanted nanobeam array can be approximated by treating the wires cross-section as N effective layers with increasing effective indices. Changing the slant angle of the sidewalls is accounted for by grading the set of effective indices with the height above the surface (see Supporting Information). The consequences of slanting are a blue-shift of the first FP reflectance minimum and a general reduction in reflection as a result of the graded-index. The red and white dashed lines of Figure 1c move closer together with increased slanting of the side walls. Note that structures with slightly slanted sidewalls perform better than both perfect structures with straight walls and completely slanted ones (see Figure 5b), which explains the low broadband reflectance that was observed experimentally. Thus, while the fabrication
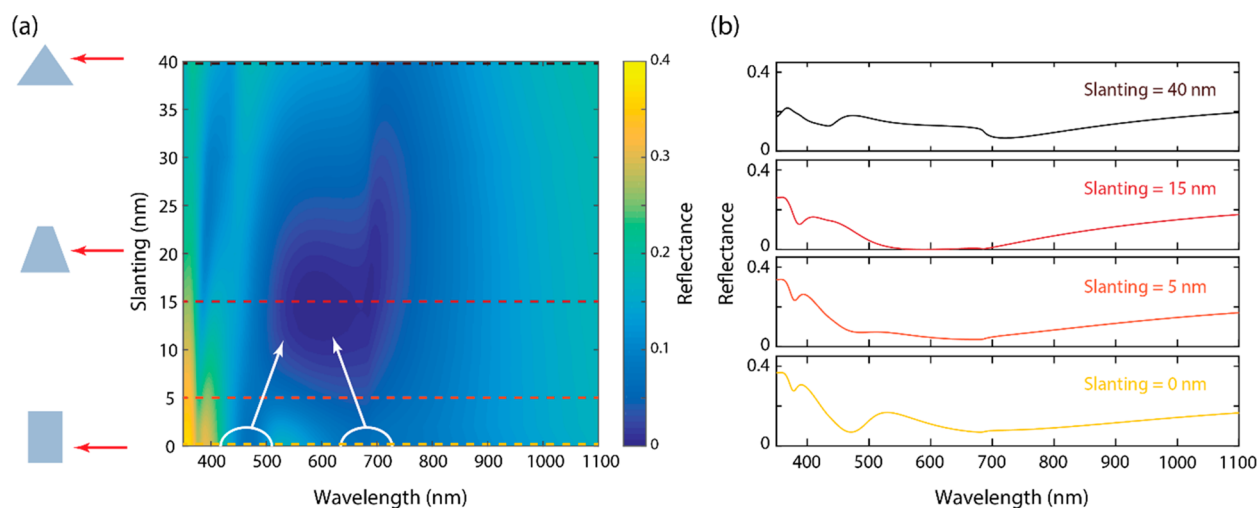
Figure 5. Impact of the sidewall slant-angle of Mie resonators on the spectral reflectance properties. (a) Dependence of the spectral reflectance (color) for an array of Si nanobeams (w = 80 nm, h = 120 nm, period 180 nm) on the slant-angle of the sidewalls. (b) Line cuts through (a) for straight walls (yellow, 0 nm slanting), 5 nm slanting (orange), 15 nm slanting (red), and 40 nm slanting (black).

imperfections make the observation of the two reflection minima more challenging, the resulting broadband lower reflectance is highly beneficial for practical applications.

CONCLUSION

In conclusion, we provide a framework to model, design, and fabricate semiconductor metafilms that combine Mie and Fabry-Pérot resonances to attain a broadband antireflection response. Specifically, we presented the working principle of our metasurfaces in a rather intuitive way supporting our explanation with CMT and showing a strong agreement between theory and FDTD simulations. Using the insights gained from CMT it is possible to optimize the interplay of the two interfering pathways by changing the structures' geometry and hence engineer a double-dip in reflection within the visible spectrum. It is important to stress that this design can be tailored not only for different materials but also for other frequency ranges, with several potential applications (solar cells, image sensors, detectors, displays components etc.). Both nanobeam- and nanopillar-arrays are fabricated and show an experimental AM1.5-averaged reflectance as low as 3.9% and 4.1% for polarized and unpolarized light, respectively. Detailed structural analysis of the fabrication imperfections and their impact on optical properties revealed that slightly slanted structures give rise to a broadening and spectral overlap of the Mie and Fabry-Pérot resonances. As a result, we can achieve even lower and more broadband antireflection performance than for structures with perfectly straight sidewalls. Finally, we note that the conceptual demonstration of multiresonant metasurface AR coatings in this work could be up-scaled to practical applications with fabrication techniques such as substrate conformal imprinting lithography,[35] nanoimprint lithography,[36] or rolling photolithography,[37] which enable large-area printing of engineered nanometer-scale structures in an inexpensive manner.

ASSOCIATED CONTENT

Ⓢ Supporting Information

The Supporting Information is available free of charge on the ACS Publications website at DOI: 10.1021/acsphotonics.8b01406.

Coupled mode theory derivation of eq 2, design routine adopted to obtain the optimized geometries, analysis of sidewalls slanting on the resonant and on the direct pathways, simulated reflection spectra as a function of the incident angle, and optical microscopy images of the samples (PDF)

AUTHOR INFORMATION

Corresponding Author

*E-mail: brongersma@stanford.edu.

ORCID Ⓘ

Andrea Cordaro: 0000-0003-3000-7943
Jorik van de Groep: 0000-0003-3033-8005
Søren Raza: 0000-0002-0296-7202
Emanuele Francesco Pecora: 0000-0003-2467-5486
Mark L. Brongersma: 0000-0003-1777-8970

Present Address

∥Center for Nanophotonics, AMOLF, Science Park 104, 1098 XG Amsterdam, The Netherlands.

Author Contributions

The manuscript was written through contributions of all authors. All authors have given approval to the final version of the manuscript.

Notes

The authors declare no competing financial interest.

REFERENCES

(1) Rayleigh, J. W. S. On reflection of vibrations at the confines of two media between which the transition is gradual. *P. London Math. Soc.* **1879**, s1−11, 51−56.

(2) Sexton, F. W. Plasma nitride AR coatings for silicon solar cells. *Sol. Energy Mater.* **1982**, *7*, 1−14.

(3) Zhao, J.; Green, M. A. Optimized antireflection coatings for high-efficiency silicon solar cells. *IEEE Trans. Electron Devices* **1991**, *38*, 1925−1934.

(4) Zhao, J.; Wang, A.; Altermatt, P.; Green, M. A. Twenty-four percent efficient silicon solar cells with double layer antireflection coatings and reduced resistance loss. *Appl. Phys. Lett.* **1995**, *66*, 3636−3638.

(5) Chhajed, S.; Schubert, M. F.; Kim, J. K.; Schubert, E. F. Nanostructured multilayer graded-index antireflection coating for Si solar cells with broadband and omnidirectional characteristics. *Appl. Phys. Lett.* **2008**, *93*, 251108.

(6) Yan, X.; Poxson, D. J.; Cho, J.; Welser, R. E.; Sood, A. K.; Kim, J. K.; Schubert, E. F. Enhanced omnidirectional photovoltaic performance of solar cells using multiple-discrete-layer tailored- and low-refractive index anti-reflection coatings. *Adv. Funct. Mater.* **2013**, *23*, 583−590.

(7) Zhu, J.; Yu, Z.; Burkhard, G. F.; Hsu, C.-M.; Connor, S. T.; Xu, Y.; Wang, Q.; McGehee, M.; Fan, S.; Cui, Y. Optical absorption enhancement in amorphous silicon nanowire and nanocone arrays. *Nano Lett.* **2009**, *9*, 279−282.

(8) Brongersma, M. L.; Cui, Y.; Fan, S. Light management for photovoltaics using high-index nanostructures. *Nat. Mater.* **2014**, *13*, 451−460.

(9) Jahani, S.; Jacob, Z. All-dielectric metamaterials. *Nat. Nanotechnol.* **2016**, *11*, 23−36.

(10) van de Groep, J.; Spinelli, P.; Polman, A. Single-step soft-imprinted large-area nanopatterned antireflection coating. *Nano Lett.* **2015**, *15*, 4223−4228.

(11) Cao, L.; Fan, P.; Vasudev, A. P.; White, J. S.; Yu, Z.; Cai, W.; Schuller, J. A.; Fan, S.; Brongersma, M. L. Semiconductor nanowire optical antenna solar absorbers. *Nano Lett.* **2010**, *10*, 439−445.

(12) Cao, L.; Fan, P.; Barnard, E. S.; Brown, A. M.; Brongersma, M. L. Tuning the color of silicon nanostructures. *Nano Lett.* **2010**, *10*, 2649−2654.

(13) Evlyukhin, A. B.; Reinhardt, C.; Seidel, A.; Luk'yanchuk, B. S.; Chichkov, B. N. Optical response features of Si-nanoparticle arrays. *Phys. Rev. B: Condens. Matter Mater. Phys.* **2010**, *82*, 045404.

(14) Kuznetsov, A. I.; Miroshnichenko, A. E.; Brongersma, M. L.; Kivshar, Y. S.; Luk'yanchuk, B. Optically resonant dielectric nanostructures. *Science* **2016**, *354*, aag2472.

(15) Bohren, C.; Huffman, D. *Absorption and Scattering of Light by Small Particles*, Wiley Science Series; Wiley, 2008.

(16) Kippenberg, T. J.; Tchebotareva, A. L.; Kalkman, J.; Polman, A.; Vahala, K. J. Purcell-factor-enhanced scattering from Si nanocrystals in an optical microcavity. *Phys. Rev. Lett.* **2009**, *103*, na.

(17) van de Groep, J.; Polman, A. Designing dielectric resonators on substrates: Combining magnetic and electric resonances. *Opt. Express* **2013**, *21*, 26285−26302.

(18) Spinelli, P.; Verschuuren, M.; Polman, A. Broadband omnidirectional antireflection coating based on subwavelength surface Mie resonators. *Nat. Commun.* **2012**, *3*, 692.

(19) Wang, Z.; Zhang, R.; Wang, S.; Lu, M.; Chen, X.; Zheng, Y.; Chen, L.; Ye, Z.; Wang, C.; Ho, K. Broadband optical absorption by tunable Mie resonances in silicon nanocone arrays. *Sci. Rep.* **2015**, *5*, 7810.

(20) Yu, Z.; Raman, A.; Fan, S. Fundamental limit of nanophotonic light trapping in solar cells. *Proc. Natl. Acad. Sci. U. S. A.* **2010**, *107*, 17491−17496.

(21) Wang, K. X.; Yu, Z.; Sandhu, S.; Fan, S. Fundamental bounds on decay rates in asymmetric single-mode optical resonators. *Opt. Lett.* **2013**, *38*, 100−102.

(22) Wang, K. X.; Yu, Z.; Sandhu, S.; Liu, V.; Fan, S. Condition for perfect antireflection by optical resonance at material interface. *Optica* **2014**, *1*, 388−395.

(23) Haus, H. *Waves and fields in optoelectronics. Prentice-Hall Series in Solid State Physical Electronics*; Prentice Hall, Inc., 1984.

(24) Fan, S.; Suh, W.; Joannopoulos, J. D. Temporal coupled-mode theory for the Fano resonance in optical resonators. *J. Opt. Soc. Am. A* **2003**, *20*, 569−572.

(25) Ruan, Z.; Fan, S. Temporal coupled-mode theory for Fano resonance in light scattering by a single obstacle. *J. Phys. Chem. C* **2010**, *114*, 7324−7329.

(26) Gaylord, T. K.; Baird, W. E.; Moharam, M. G. Zero-reflectivity high spatial-frequency rectangular-groove dielectric surface-relief gratings. *Appl. Opt.* **1986**, *25*, 4562−4567.

(27) Brundrett, D. L.; Glytsis, E. N.; Gaylord, T. K. Homogeneous layer models for high-spatial-frequency dielectric surface-relief gratings: conical diffraction and antireflection designs. *Appl. Opt.* **1994**, *33*, 2695−2706.

(28) Motamedi, M. E.; Southwell, W. H.; Gunning, W. J. Antireflection surfaces in silicon using binary optics technology. *Appl. Opt.* **1992**, *31*, 4371−4376.

(29) Landreman, P. E.; Chalabi, H.; Park, J.; Brongersma, M. L. Fabry-Perot description for Mie resonances of rectangular dielectric nanowire optical resonators. *Opt. Express* **2016**, *24*, 29760−29772.

(30) Lumerical Inc. http://www.lumerical.com/tcad-products/fdtd/

(31) Fano, U. Sullo spettro di assorbimento dei gas nobili presso il limite dello spettro d'arco. *Nuovo Cimento* **1935**, *12*, 154−161.

(32) Miroshnichenko, A. E.; Flach, S.; Kivshar, Y. S. Fano resonances in nanoscale structures. *Rev. Mod. Phys.* **2010**, *82*, 2257−2298.

(33) Luk'yanchuk, B.; Zheludev, N. I.; Maier, S. A.; Halas, N. J.; Nordlander, P.; Giessen, H.; Chong, C. T. The Fano resonance in plasmonic nanostructures and metamaterials. *Nat. Mater.* **2010**, *9*, 707−715.

(34) Palik, E. *Handbook of Optical Constants of Solids*; Academic Press, 1998.

(35) Verschuuren, M. A.; Megens, M.; Ni, Y.; van Sprang, H.; Polman, A. Large area nanoimprint by substrate conformal imprint lithography (SCIL). *Adv. Opt. Technol.* **2017**, *6*, 243−264.

(36) Chou, S. Y.; Krauss, P. R.; Renstrom, P. J. Nanoimprint lithography. *J. Vac. Sci. Technol., B: Microelectron. Process. Phenom.* **1996**, *14*, 4129−4133.

(37) Kobrin, B.; Barnard, E. S.; Brongersma, M. L.; Kwak, M. K.; Guo, L. J. Rolling mask nanolithography: the pathway to large area and low-cost nanofabrication. *Proc. SPIE* **2012**, *8249*, 82490O.